RSC Advances

PAPER

View Article Online
View Journal | View Issue

Cite this: *RSC Adv.*, 2021, **11**, 15738

Green synthesis of nitrogen-doped multiporous carbons for oxygen reduction reaction using water-caltrop shells and eggshell waste

Chun-Han Hsu, †[a] Zheng-Bang Pan,†[b] Hau-Ting Qu,[b] Chuan-Ren Chen,[b] Hong-Ping Lin, *[b] I-Wen Sun,*[b] Ching-Ying Huang[c] and Chun-Han Li[c]

Received 16th March 2021
Accepted 22nd April 2021

DOI: 10.1039/d1ra02100a

rsc.li/rsc-advances

A green synthesis method is proposed for the preparation of nitrogen-doped multiporous carbons (denoted as N-MPCs) from water-caltrop shell (WCS) using eggshell waste as both a nitrogen-dopant and an activating agent. It is shown that the surface area, porosity, yield and nitrogen content of the as-prepared N-MPCs can be easily controlled by adjusting the activation temperature. Moreover, in oxygen reduction reaction (ORR) tests performed in O_2-saturated 0.1 M $KOH_{(aq)}$ electrolyte containing 1.0 M methanol, the N-MPC catalysts show a high ORR stability and good resistance to methanol corrosion. In addition, as a cathode material in Al–air battery tests, the N-MPCs achieve a power density of 16 mW g^{-1} in a saturated $NaCl_{(aq)}$ electrolyte. Overall, the results show that the N-MPCs have a promising potential as a green and sustainable material for ORR catalysis applications.

1. Introduction

As electric vehicles continue to develop and become more widespread, fuel cells and metal–air batteries have emerged as a mainstream technology for automotive applications.[1–4] However, the performance of modern fuel cells and metal–air batteries is limited by the slow reaction rate of the oxygen reduction reaction (ORR) at the cathode.[5,6] Although this problem can be solved by using Pt catalysts to enhance the ORR activity, Pt is expensive, lacks sufficient durability, and has low natural abundance.[7,8]

Accordingly reducing Pt-based electrodes in fuel cells and metal–air batteries has attracted significant attention in recent years and has led to the development of many new ORR electrocatalyst materials, including non-noble metal catalysts,[9] carbon-supported metal composites,[10] organic macrocycles,[11] and nitrogen-doped carbons.[12] Among these catalyst materials, nitrogen-doped carbons have many advantages, including high electrical conductivity, nanoporous structures, high stability and strong catalytic activity.[13–15] Notably, this enhanced performance is evident under both neutral and alkaline pH conditions.[16] However, most existing methods for preparing nitrogen-doped carbon materials, *e.g.*, the thermal decomposition of nitrogen-containing precursors over metals such as Fe, Co and Ni, lead to the presence of residual metal species or impurities in the synthesized carbons, which seriously degrade the ORR performance.[17–20] Several recent studies have shown that nitrogen-doped carbons can be prepared as an electrocatalyst material for ORR without any metal precursors.[21,22] Thus, metal-free materials, including nitrogen-doped carbons, have attracted growing interest as a catalyst material in recent years on account of their excellent ORR electrochemical properties, low cost, low side-reaction effects and good stability.[23]

Eggshell is a mainly inorganic material; consisting of approximately 95 wt% $CaCO_3$ and 3.5 wt% protein organic matrix.[24] Around 7 billion eggs are consumed in Taiwan each year, and the majority of the eggshells are simply thrown away. If the eggshells were recycled and reused, this would not only ease the environmental impact, but would also create a valuable green chemical resource. In a previous study, the present group proposed an economic, sustainable and green synthesis method for preparing multiporous carbons (denoted as MPCs) from waste water-caltrop shell (denoted as WCSs) using commercial $CaCO_3$ nanoparticles as a template.[25] The WCS have been carbonized already to biochar by using a top-lit-updraft method.[25] In the proposed method, the $CaCO_3$ nanoparticles served both act as a spacer and an activating agent for the WCS biochar. In many previous reports, nitrogen-containing compounds, such as melamine,[26] chitosan,[27] or urea,[28] have been used to react with the carbon source under high temperature conditions to produce nitrogen-doped carbons. In the present study, it is speculated that eggshell waste can serve as both a template and an activating agent in place of the $CaCO_3$ and nitrogen-containing compounds used in traditional MPC synthesis routes.

Accordingly, the present study prepares nitrogen-doped MPC (N-MPC) using eggshell waste as a nitrogen-dopant and carbon-

[a]*General Education Center, National Tainan Junior College of Nursing, Tainan 700, Taiwan*

[b]*Department of Chemistry, National Cheng Kung University, Tainan 70101, Taiwan. E-mail: hplin@mail.ncku.edu.tw; iwsun@mail.ncku.edu.tw; Fax: +886-6-276 2331; Tel: +886-6-275 7575#65342*

[c]*Green Energy and Environment Research Laboratories, Industrial Technology Research Institute, Tainan 71150, Taiwan*

† Zheng-Bang Pan and Chun-Han Hsu contributed equally to this work.

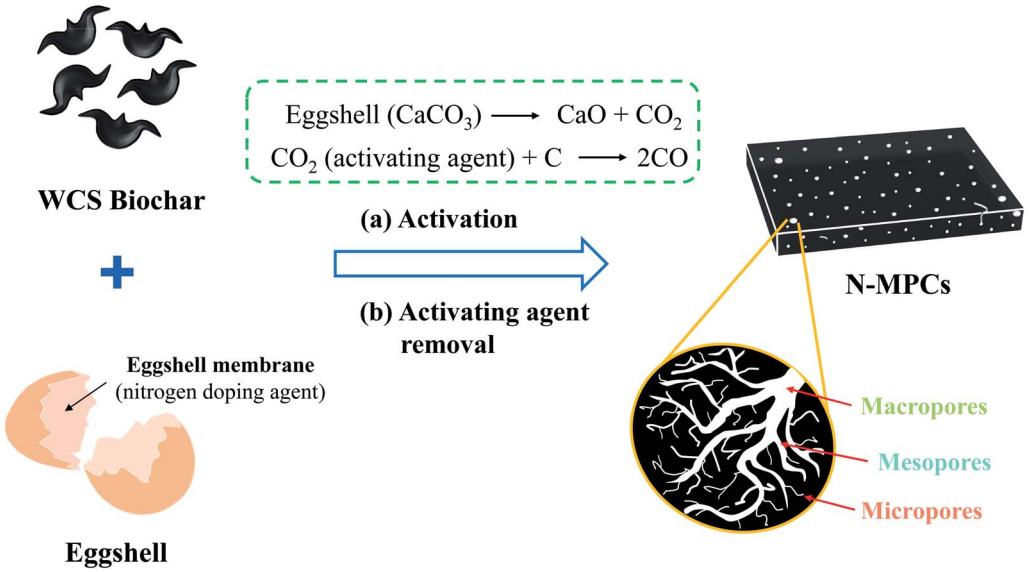

Fig. 1 Schematic illustration of synthesis for N-MPC material.

activating agent, and the WCS biochar (WCSB) as the carbon source (see Fig. 1). The thermal stability, microstructure, morphology and electrochemical properties of the resulting N-MPCs are investigated for various activation temperatures in the range of 800–950 °C. The practical application of the synthesized N-MPCs as a cathode catalyst material for ORR is then evaluated both directly in O_2-saturated 0.1 M $KOH_{(aq)}$ electrolyte containing 1.0 M methanol and in Al–air battery tests performed with saturated $NaCl_{(aq)}$ electrolyte.

2. Experimental section

2.1 Synthesis of N-MPCs *via* physical blending method

WCSB (surface area >200 $m^2\ g^{-1}$) were purchased from FanC Recycling International Ltd., Taiwan.[25] To synthesize the N-MPCs, 8.0 g of the WCSB, 8.0 g K_2CO_3 and 16.0 g of the eggshell waste were homogeneously ground and mixed in a blender (Lab Use Grinder, SRT-02, Fu-Lian Food Machinery) for 3 minutes. The resulting powder was sealed in a stainless-steel container (150 mL), heated to a temperature of 750 °C at a heating rate of 8 °C min^{-1} for 2 h and then activated at higher temperatures in the range of 800–950 °C for 3 h. After cooling to room temperature, the black powder was washed with water to remove the alkali salt and then immersed in 1.0 M $HCl_{(aq)}$ solution to remove the residual $Ca(OH)_2$ and other inorganic residues. After stirring overnight under pH conditions of less than 1.0, the solution was filtered, and the product was washed repeatedly with DI water. The resulting N-MPCs were dried at 100 °C until required for testing and analysis. For comparison purposes, additional samples were also prepared using only WCSB and K_2CO_3 or WCSB and eggshell, respectively, (see MPC–K_2CO_3 and MPC–eggshell in Table 1). Both samples were activated at a temperature of 900 °C.

2.2 Characterizations

The thermal stability of the various samples was characterized using a thermal gravimetric analyzer (TA Instruments Q50, USA) at temperatures of 100–800 °C and a ramp rate of 20 °C min^{-1} under an air atmosphere. The specific surface areas of the MPCs were determined from the nitrogen sorption isotherms acquired by a Micromeritics Tristar II 3020 surface area analyzer using the Brunauer–Emmett–Teller (BET) method. The XRD patterns of the N-MPCs activated at different temperatures were recorded with an X-ray diffractometer (Rigaku MultiFlex) (40 kV, 20 mA) using Cu Kα radiation. The carbon structures of the samples were identified using a Renishaw micro- Raman spectrometer using a He–Ne laser source with a wavelength of

Table 1 Textural properties, structure properties and yield of MPC samples prepared using different activation temperatures

Sample	S_{BET}[a]/$m^2\ g^{-1}$	S_{Mic}[b]/$m^2\ g^{-1}$	S_{Meso}[c]/$m^2\ g^{-1}$	S_{Meso}/S_{BET}	Nitrogen content[d]/wt%	Yield/%
Biochar	292	259	33	13%	1.2	—
MPC–K_2CO_3	836	697	139	17%	—	51
MPC–eggshell	677	394	283	58%	—	68
N-MPC-800	839	459	380	45%	4.3	39
N-MPC-900	1273	660	593	47%	3.8	31
N-MPC-950	1524	737	787	52%	3.4	28
MPC	1499	584	915	61%	1.1	31

[a] BET surface area. [b] Micropore surface area. [c] Mesoporous surface area. [d] Nitrogen content is from elemental analysis.

633 nm. The morphologies of the MPC samples were characterized using a JEOL JEM6700 field emission scanning electron microscope (FESEM) with an operating voltage of 10 kV. The pore structures of the various samples were observed using a JEM-2100F Electron Microscope (HR-TEM) with an accelerating voltage of 200 kV. Finally, X-ray photoelectron spectroscopy (XPS) measurements were conducted using a VG Scientific ESCALAB 210 electron spectrometer with Mg Kα radiation and a vacuum of 2×10^{-8} Pa.

2.3 Electrochemical measurements

Electrochemical measurements were taken using a CHI-608A potentiostat/galvanostat and a conventional three-electrode test cell. 5.0 mg MPCs, 20 μL polytetrafluoroethylene (PTFE, Sigma-Aldrich, 5 wt% dispersion in water) and 1.0 mL *N*-methyl-2-pyrrolidone (NMP) were uniformly mixed to form a carbon slurry. 20 μL of the slurry was dropped onto a glassy carbon electrode (5 mm diameter, Pine) and left to dry under room temperature conditions. An aliquot of catalyst suspension was then transferred onto a carbon substrate; resulting in a catalyst loading of 0.51 mg catalyst cm^{-2}. Cyclic voltammetry (CV) tests were performed over a voltage range of −1.0 to 0.2 V using an Ag/AgCl reference electrode and O_2-saturated 0.1 M KOH electrolyte solution. The measured potentials *vs.* Ag/AgCl were converted to the reversible hydrogen electrode (RHE) scale according to the Nernst equation. Following the CV tests, linear sweep voltammograms (LSVs) were obtained using a rotating disk electrode (RDE) with rotation rates in the range of 400–3000 rpm. All the electrochemical measurements were performed using a scan rate of 0.01 V s^{-1}.

3. Results and discussion

3.1 N-MPC samples prepared using different activation temperatures

Fig. 2(a) shows the thermal gravimetric analysis (TGA) curves of pure WCSB, pure eggshell, and the WCSB/eggshell blend, respectively. As shown, the eggshell, which consists mainly consisted of $CaCO_3$, begins to decompose and form CaO and CO_2 at a temperature of approximately 650 °C. It is well known that CO_2 reacts with carbon materials at a high temperatures (*e.g.*, 850 °C);[29] and thereby increasing their porosity. Accordingly, the present study deliberately adopted a two-stage thermal treatment process for activation and nitrogen-doping to synthesize the desired N-MPCs. In particular, an initial activation and nitrogen-doping process was performed at 750 °C to completely decompose the $CaCO_3$ to generate CO_2 and convert the proteins in the eggshell waste to nitrogen-doping components for insertion into the carbon structure. A second activation process was then performed at a higher temperature in the range of 800–950 °C to enhance the

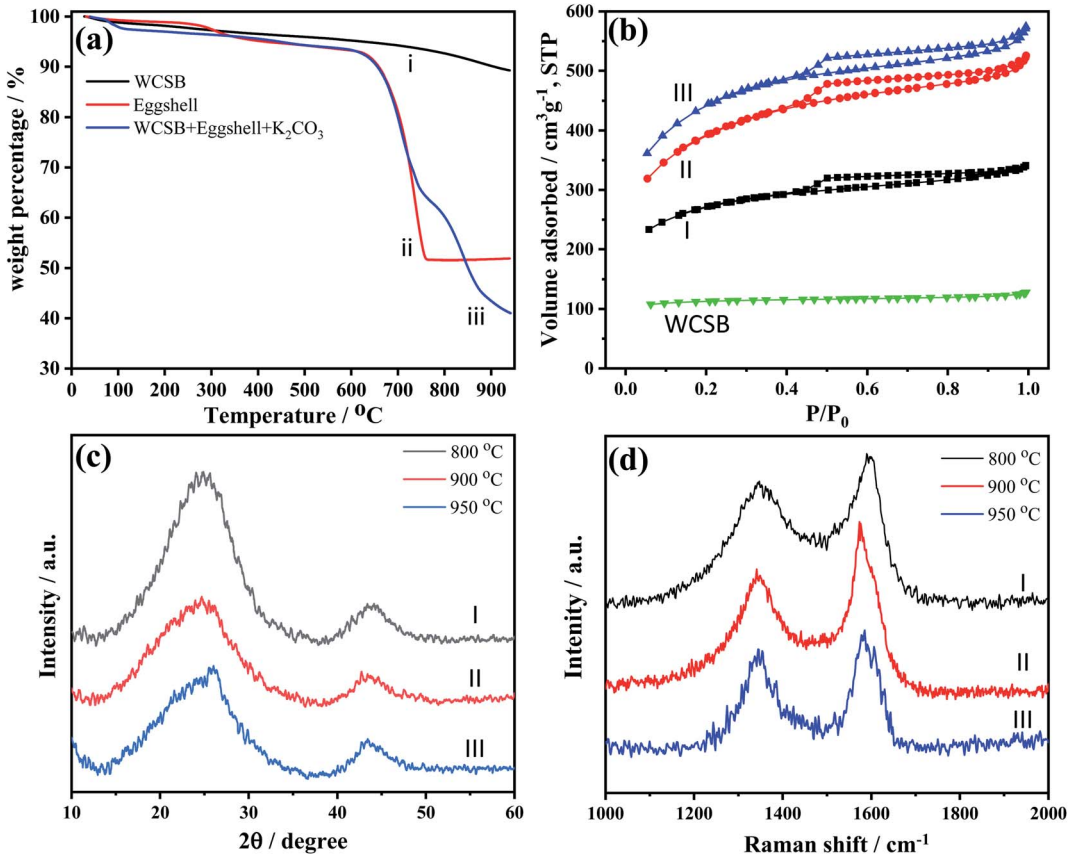

Fig. 2 (a) TGA curves for WCSB (i), eggshell (ii) and WCSB/eggshell blend (iii). (b) Nitrogen sorption isotherms. (c) XRD patterns and (d) Raman spectra for N-MPC samples prepared using activation temperatures of (I) 800 °C, (II) 900 °C and (III) 950 °C.

reaction of the added K_2CO_3 with the carbon to form porous carbons with a large surface area and high porosity.[25,29] It is noted that while a higher temperature is beneficial in increasing the surface area and pore volume of the resulting porous carbons, it decreases the nitrogen content and product yield.[26–28] Thus, in practice, an appropriate choice of the activation temperature is essential in optimizing the porous properties of the obtained N-MPCs.

As shown in Fig. 2(b), the N_2 adsorption–desorption plots of all the N-MPC components exhibit type-IV isotherms; indicating the existence of mesopores in every component. The BET surface area of the biochar was found to increase from 292 m^2 g^{-1} in the pristine (*i.e.*, non-activated) condition to 839–1524 m^2 g^{-1} in the synthesized N-MPC condition (see Table 1). Furthermore, both the surface area and the ratio of the meso-/micropore surface area of the N-MPCs increased with an increasing activation temperature due to the improved activation effect of the CO_2 at higher temperatures.[30,31] Notably, the use of eggshell as the nitrogen precursor allowed the nitrogen wt% content of the N-MPCs to be easily adjusted in the range of 3.4–4.3 wt% simply by controlling the activation temperature. When using only K_2CO_3 as the activating agent (*i.e.*, MPC–K_2CO_3 in Table 1), the sample had a BET surface area of 836 m^2 g^{-1}. However, the mesoporous surface area ratio had a low value of 17% despite the relatively high activation temperature of 900 °C. By contrast, the use of only eggshell waste as the activating agent resulted in a much higher mesoporous surface area ratio of 48% to 52%. In other words, the eggshell waste served not only as an effective N-dopant, but also as an effective means of enhancing the mesoporosity of the porous carbons. Overall, the results presented in Table 1 show that an activation temperature of 900 °C yields an N-MPC material with a large specific surface area (1273 m^2 g^{-1}), an acceptable yield (31%) and a high nitrogen content (3.8 wt%).

Fig. 2(c) presents the X-ray diffraction (XRD) patterns of the N-MPCs prepared with different activation temperatures. All of the patterns exhibit broad diffraction peaks centered at $2\theta \approx 25^\circ$ and 43°, respectively, which suggests a graphite structure with (002) and (100) crystal planes.[32] As the activation temperature increases, the width of the peak at $2\theta \approx 25^\circ$ broadens and the intensity reduces. In other words, a higher activation temperature prompts a lower crystallinity of the N-MPCs, which leads in turn to a higher porosity and surface area of the porous carbons. Usually, higher temperatures result in increased graphitization, *i.e.*, higher crystallinity. However, in the present study, a higher temperature increases the porosity of the prepared material due to activation with CO_2 and a greater number of defects, and decreases the crystallinity accordingly.

The degree of graphitization of the N-MPC samples was further analyzed by Raman spectroscopy, as shown in Fig. 2(d). According to previous studies,[33] the Raman spectra of carbon materials show two broad peaks near 1350 cm^{-1} and 1580 cm^{-1} corresponding to the D-band and G-band of the carbon structure, respectively. The D-band arises from disordered sp^3 hybridized carbon, while the G-band is associated with highly ordered pyrolytic graphite, and indicates the presence of sp^2 hybridized carbon. The extent of defects in carbon materials can be quantified by the intensity ratio of the D to G bands (*i.e.*, I_D/I_G).[34] In particular, a small value of the I_D/I_G ratio implies an improved graphitization (*i.e.*, a lower number of defects). An inspection of Fig. 2(d) shows that, for the present N-MPC samples, the I_D/I_G ratio has values of 0.82, 0.72 and 0.83 for

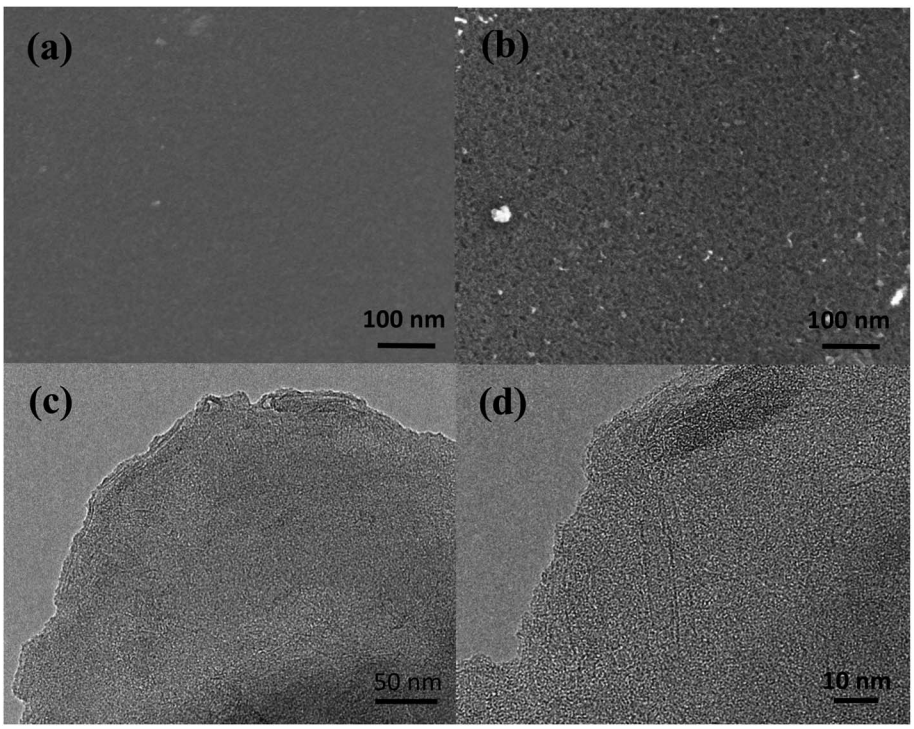

Fig. 3 (a) SEM image for WCSB; (b) SEM image and (c), (d) TEM images of N-MPC material.

activation temperatures of 800 °C, 900 °C and 950 °C, respectively. In other words, the maximum degree of graphitization is obtained at an activation temperature of 900 °C. As the temperature is further increased to 950 °C, the surface area increases as a result of the higher activation efficiency. Consequently, the degree of defects also increases and causes the I_D/I_G value to rise accordingly.

Fig. 3(a) and (b) show SEM images of the WCSB and N-MPC samples carbonized at 900 °C, respectively. The WCSB sample has a smooth surface (even under high magnification), as shown in Fig. 3(a). However, the N-MPCs have a porous structure with a nanometer scale, as shown in Fig. 3(b). In addition, a detailed inspection of the TEM image presented in Fig. 3(c) shows that the N-MPCs have a highly porous structure. The higher-magnification image presented in Fig. 3(d) reveals that the N-MPCs have a worm-like structure and contain some lattice stripes of graphite. The irregular arrangement of the worm-like structure indicates that the N-MPCs have an amorphous structure.

The chemical structure of the N-MPCs synthesized at 900 °C was analyzed by XPS. The XPS spectra presented in Fig. 4(a) and (b) show the presence of an N 1s peak (~398 eV) in addition to a C 1s peak (~285 eV), and therefore confirm the successful doping of nitrogen in the synthesized material. However, in addition to carbon and nitrogen, the N-MPCs also contain many oxygen-containing functional groups, as evidenced by the O 1s peak located at around 532 eV in Fig. 4(c). The atomic percentages of C, N and O are determined to be 90%, 2.4% and 7.6%, respectively. Notably, the high-resolution N 1s XPS spectrum presented in Fig. 4(d) shows that the N-MPCs not only contain pyridinic-N (398.3 eV) and pyrrolic-N (399.8 eV), but also graphitic-N (401.3 eV) and oxidized-N (403.7 eV). According to previous studies,[35] a mixed pyridinic-N and graphitic-N structure is beneficial in enhancing the catalytic activity of carbon toward ORR. Accordingly, the ORR activities of the biochar, MPCs and N-MPCs were further evaluated and compared, as discussed in the following sub-section.

3.2 Electrochemical catalytic activity of N-MPC samples

The ORR electrocatalytic performance of the biochar, MPC and N-MPC materials was measured in alkaline electrolyte (0.1 M KOH). The tests commenced by measuring the activity of the N-MPCs in saturated O_2 and N_2 environments by means of CV tests. As shown in Fig. 5(a), the N-MPCs exhibited a strong catalytic performance for ORR in the O_2-saturated 0.1 M KOH environment, but only a weak performance in the saturated N_2 environment. Neither CV curve shows any additional reduction peaks. Hence, it is inferred that the N-MPCs have good stability and initiate no side-reactions. As shown in Table 1, the WCSB and MPCs both contain nitrogen elements due to the nitrogen content of the pristine WCS. Therefore, the ORR catalytic activity of both materials was also measured for comparison purposes, as shown in Fig. 5(b). For both materials, oxygen reduction peaks are observed; indicating a strong catalytic activity. Generally speaking, the intensity of the ORR reaction activity can be judged by the initial reaction potential and current density of the CV curve. Thus, observing Fig. 5(b), it is found that, of the three materials, the N-MPCs exhibit the best catalytic performance, with the highest initial potential (0.10 V *vs.* RHE) and current density (0.74 mA cm^{-2}) (see Table 2). It is additionally noted that the MPCs have a higher initial potential and current density (0.05 V, 0.58 mA

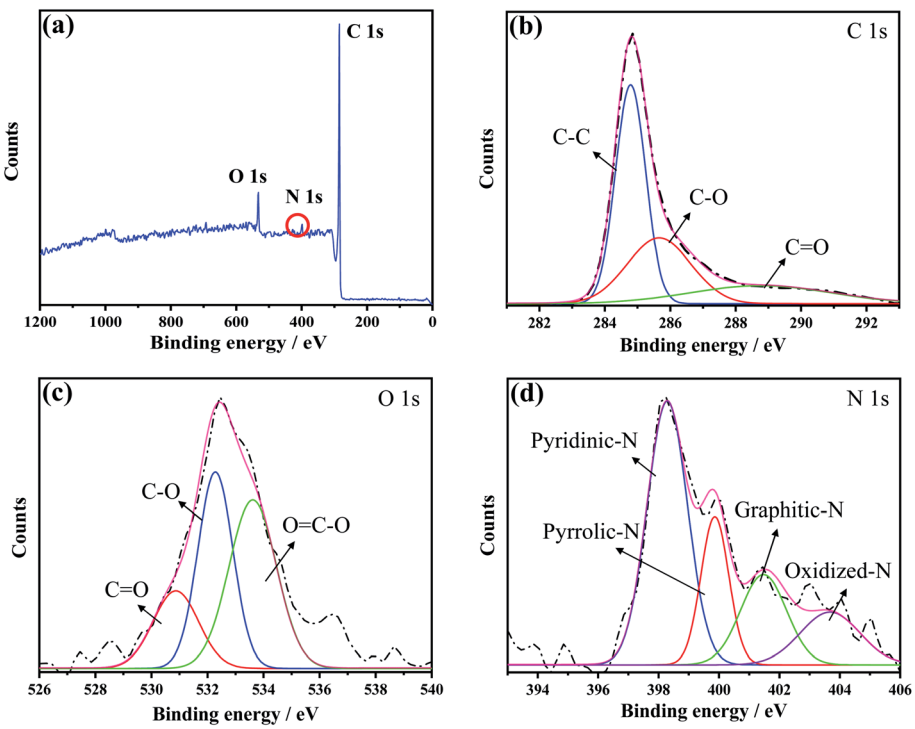

Fig. 4 XPS analysis results for C 1s, O 1s and N 1s binding energies of N-MPC material.

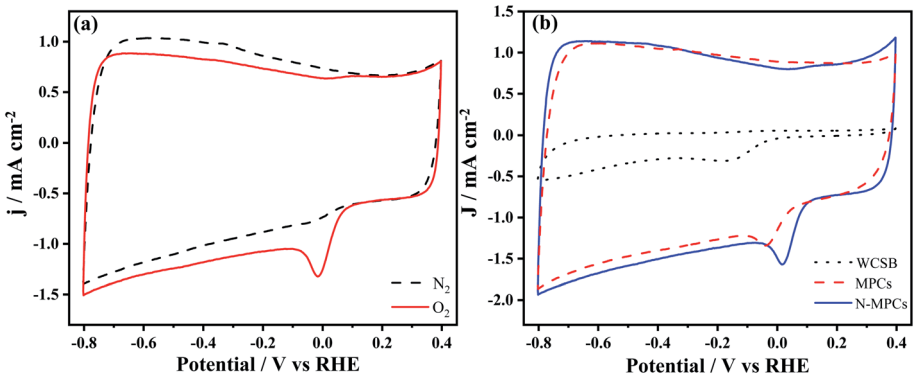

Fig. 5 CV curves for (a) N-MPC in N_2- and O_2-saturated 0.1 M $KOH_{(aq)}$, and (b) WCSB, MPC and N-MPC in O_2-saturated 0.1 M $KOH_{(aq)}$. Note that scan rate is 0.01 V s^{-1} in every case.

Table 2 Catalytic performance of various samples in ORR and Al–air battery tests

	ORR		Al–air battery	
Sample	Onset potential/V	Current density/mA cm^{-2}	Initial voltage/V	Initial current/A
Biochar	−0.03	0.04	0.50	0.03
MPC	0.05	0.58	0.80	0.25
N-MPC	0.10	0.74	0.91	0.39

cm^{-2}) than the biochar (−0.03 V, 0.04 mA cm^{-2}). It is hence inferred that the increased surface area of the MPCs exposes a greater number of active sites to the reactant and therefore improves the overall catalytic performance.

The catalytic efficiency of the N-MPCs for ORR was further studied using an LSV and rotating disk electrode (RDE) voltammetry technique with different rotation speeds in the range of 400–3000 rpm. As shown in Fig. 6(a), as the rotation speed increased, the diffusion-limited current density also increased.[36] It is hence inferred that a higher rotation speed results in a thinner diffusion layer, which allows the oxygen in the N-MPCs to diffuse to the electrode surface more rapidly, and hence increases the reaction current.

The number of electrons transferred during ORR can be determined from the LSV measurements obtained at different rotation speeds using the following Koutecky–Levich (K–L) equation:[37]

$$1/J = 1/J_K + 1/J_L = 1/J_K + 1/(B\omega^{0.5}) \quad (1)$$

$$B = 0.2nFC_0(D_0)^{2/3}v^{-1/6} \quad (2)$$

where J is the measured current density, J_K is the kinetic current density, J_L is the limiting diffusion current density, ω (rpm) is the electrode rotation speed, n is the number of electron transfers per oxygen molecule, and F is the Faraday constant (96 485 C mol^{-1}). In addition, C_0 is the bulk concentration of oxygen (1.2×10^{-3} M), D_0 is the diffusion coefficient of oxygen (1.9×10^{-5} cm^2 s^{-1}), and v is the kinematic viscosity of the electrolyte (1.0×10^{-2} cm^2 s^{-1}). Fig. 6(b) shows the K–L plot for Fig. 6(a), where the number of electrons transferred at each voltage is indicated in the lower-right corner of the figure. (Note that the number of electrons is determined from the slope of the corresponding K–L plot.) The average number of electron transfers

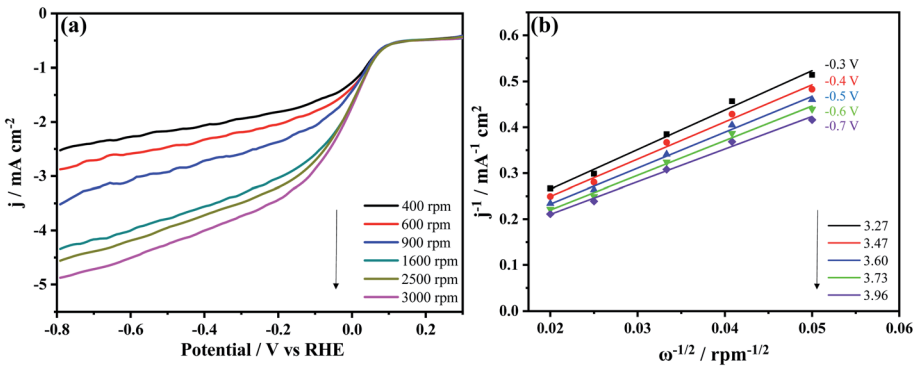

Fig. 6 (a) LSV curves for N-MPC obtained at rotation speeds of 400–3000 rpm, and (b) related K–L plot. Note that LSV tests are performed in O_2-saturated 0.1 M $KOH_{(aq)}$ electrolyte with scan rate of 0.01 V s^{-1}.

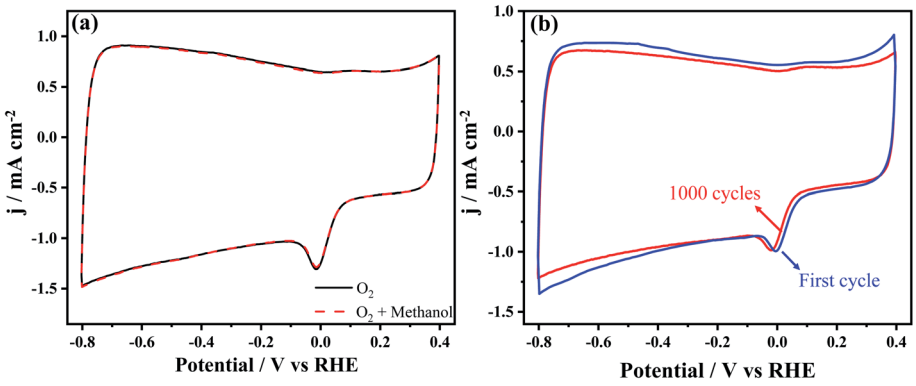

Fig. 7 CV curves for (a) N-MPC in O_2-saturated 0.1 M $KOH_{(aq)}$ and O_2-saturated 0.1 M $KOH_{(aq)}$ containing 1.0 M methanol, and (b) durability test of N-MPC in O_2-saturated 0.1 M $KOH_{(aq)}$. Note that scan rate is 0.01 V s^{-1} in both cases.

is seen to be 3.6. Generally, in fuel cells, it is expected that the ORR reaction occurs through a four-electron transfer process, which is conducive to increasing the reaction rate and providing more power.[21,23] Overall, the results presented in Fig. 5 and 6 confirm that the present N-MPCs have a high activity in ORR and are consistent with this expected reaction mechanism.

In catalytic reactions, the stability of the catalyst is one of the most important factors affecting the entire reaction system. Generally, in direct methanol fuel cells, the concentration gradient prompts molecular diffusion or electroosmotic drag, which causes the methanol to penetrate the proton exchange membrane from the anode side to the cathode side.[38] Many studies have shown that commercial ORR catalysts (Pt/C) have a low catalytic activity for oxygen reduction due to the methanol cross-over effect, and therefore limit the performance of the fuel cell.[39–41] Consequently, the stability and resistance of the present N-MPCs to the methanol cross-over effect was investigated by adding 5.0 mL of methanol to the test electrolyte (150 mL of 0.1 M KOH). The resulting CV curve (see Fig. 7(a)) shows no obvious change or additional redox peaks compared to the original curve. In other words, the catalytic performance of the N-MPCs is robust to the methanol cross-over effect. To verify the stability of the N-MPC catalyst, the CV curves were plotted over 1000 continuous cycles. As shown in Fig. 7(b), the CV curve after 1000 cycles was very similar to that after the initial cycle. Hence, the catalytic activity stability of the N-MPCs in ORR was confirmed.

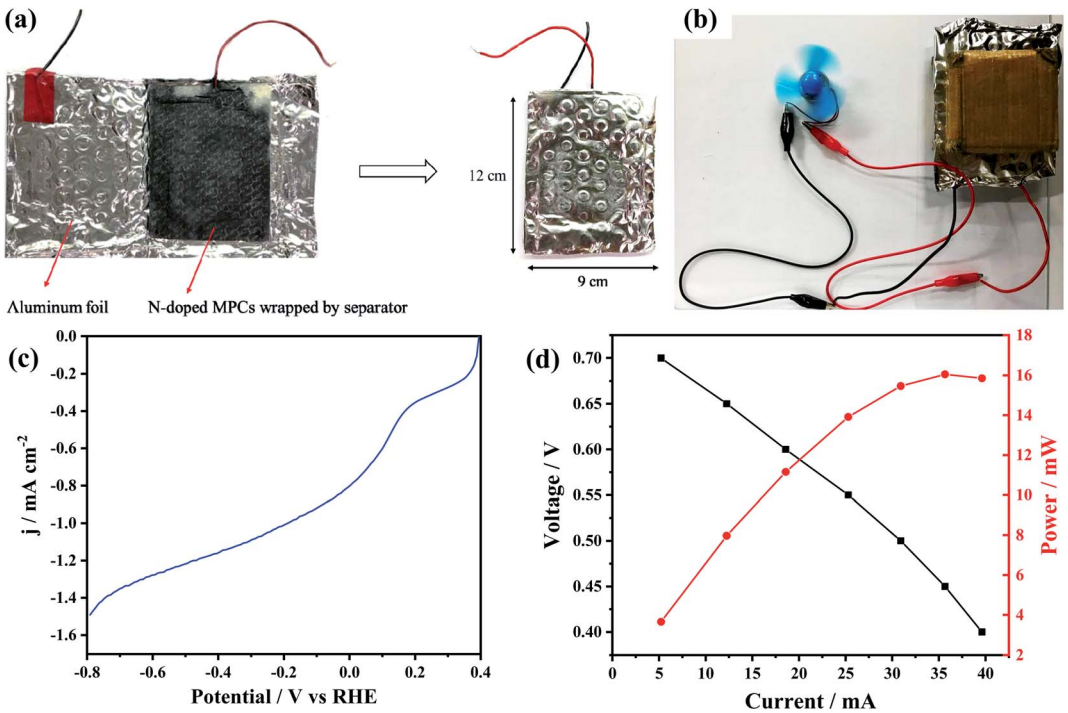

Fig. 8 Photographs of (a) assembled Al–air battery and (b) Al–air battery-mechanical motor demonstration module. (c) LSV curve for N-MPC obtained at rotation speed of 2500 rpm in O_2 saturated $NaCl_{(aq)}$ and 0.01 V s^{-1} scan rate. (d) Polarization curve and power density of Al–air battery.

3.3 Aluminum–air battery performance of N-MPCs as cathode material

Metal–air batteries have a theoretical energy density much higher than that of existing batteries (*e.g.*, lithium batteries, lead–acid batteries, and so on), and have thus attracted significant attention in the literature.[42,43] Accordingly, the present study fabricated three Al–air batteries using N-MPC, WCSB and MPC as cathode materials, respectively, and saturated $NaCl_{(aq)}$ aqueous solution as the electrolyte (see Fig. 8(a)). As shown in Fig. 8(b), each battery was assembled with a motor for demonstration purposes. Among the three batteries, that with the N-MPC cathode exhibited the highest initial voltage (0.91 V) and current (0.39 A), as shown in Table 2. The LSV curve (Fig. 8(c)) similarly exhibited a high catalytic performance, with a high initial potential (0.10 V *vs.* RHE) and current density (1.5 mA cm^{-2}). The performance of the N-MPCs is similar to that reported in the literature for other nitrogen-containing carbon materials for ORR.[43–45] Fig. 8(d) shows the polarization curve and power density curve of the Al–air battery with the N-MPC cathode. As shown, the N-MPC cathode developed a maximum power density of 16 mW g^{-1}, which enabled the motor to be driven for more than 4 h. The enhanced electrocatalytic activity of the N-MPC catalyst can be tentatively explained as follows: (1) the high surface area and accessibility of the N-MPCs increase the availability of enhanced reaction sites, (2) the nitrogen-doped sites serve as effective oxygen reaction activation sites, and (3) the low number of structural defects results in an improved electrical conductivity. Notably, the second point suggests that the presence of nitrogen species in the high surface area N-MPC catalyst plays an important role in enhancing the reaction activity of the catalyst for ORR.

4. Conclusions

N-MPCs have been successfully synthesized by activated WCSB with eggshell waste. It has been shown that the N-MPC nanocomposites activated at a temperature of 900 °C have a high surface area (>1200 m^2 g^{-1}) and a low number of structural defects. Moreover, the N-MPCs have a mixed pyridinic-N and graphitic-N structure with a N content of 3.8 wt%. In electrocatalytic ORR activity tests, the N-MPCs have shown a high electrocatalytic activity with an average electron transfer number of 3.6 in alkaline $NaOH_{(aq)}$ electrolyte. Furthermore, when used as the cathode material in an Al–air battery, the N-MPCs have exhibited a maximum power density of 16 mW g^{-1} and have enabled a small motor to be driven for more than 4 h. Overall, the N-MPCs synthesized in the present study are obtained through a simple, scalable and green route and have significant potential as a future cathode material for ORR electrodes in energy conversion devices.

Conflicts of interest

There are no conflicts to declare.

Acknowledgements

This work was financially supported by the Bureau of Energy of the Ministry of Economic Affairs of Taiwan under the project "Development of High Efficiency Hydrogen Energy and Fuel Cell Technology" (108-D0111). The authors gratefully acknowledge the use of JEOL JEM-2100F Cs STEM equipment belonging to the Core Facility Center of National Cheng Kung University.

References

1 Q.-Q. Zhang and J.-Q. Guan, Single-atom catalysts for electrocatalytic applications, *Adv. Funct. Mater.*, 2020, **30**, 2000768.
2 A. González, E. Goikolea, J. A. Barrena and R. Mysyk, Review on supercapacitors: technologies and materials, *Renewable Sustainable Energy Rev.*, 2016, **58**, 1189–1206.
3 L. Yang, J. Shui, L. Du, Y. Shao, J. Liu, L. Dai and Z. Hu, Carbon-based metal-free ORR electrocatalysts for fuel cells: past, present, and future, *Adv. Mater.*, 2019, **31**, e1804799.
4 Z. Chen, H. Zhuo, Y. Hu, L. Zhong, X. Peng, S. Jing, Q. Liu, X. Zhang, C. Liu and R. Sun, Self-biotemplate preparation of hierarchical porous carbon with rational mesopore ratio and high oxygen content for an ultrahigh energy-density supercapacitor, *ACS Sustainable Chem. Eng.*, 2018, **6**, 7138–7150.
5 X.-D. Wen, Q.-Q. Zang and J.-G. Guan, Applications of metal–organic framework-derived materials in fuel cells and metal–air batteries, *Coord. Chem. Rev.*, 2020, **409**, 213214.
6 S. Gao, X. Li, L. Li and X. Wei, A versatile biomass derived carbon material for oxygen reduction reaction, supercapacitors and oil/water separation, *Nano Energy*, 2017, **33**, 334–342.
7 C.-H. Hsu, J.-Y. Jan, H. P. Lin and P.-L. Kuo, Nitrogen-doped mesoporous carbon hollow sphere as novel carbon support for oxygen reduction reaction, *New J. Chem.*, 2014, **38**, 5521–5526.
8 C.-H. Hsu and P.-L. Kuo, The use of carbon nanotubes coated with a porous nitrogen-doped carbon layer with embedded Pt for the methanol oxidation reaction, *J. Power Sources*, 2012, **198**, 83–89.
9 S. N. S. Goubert-Renaudin and A. Wieckowski, Ni and/or Co nanoparticles as catalysts for oxygen reduction reaction (ORR) at room temperature, *J. Electroanal. Chem.*, 2011, **652**, 44–51.
10 H. Xia, Y. Wang, J. Lin and L. Lu, Hydrothermal synthesis of MnO_2/CNT nanocomposite with a CNT core/porous MnO_2 sheath hierarchy architecture for supercapacitors, *Nanoscale Res. Lett.*, 2012, **7**, 33.
11 S. Yamazaki, M. Asahi and T. Ioroi, Promotion of oxygen reduction on a porphyrazine-modified Pt catalyst surface, *Electrochim. Acta*, 2019, **297**, 725–734.
12 H.-F. Wang, C. Tang and Q. Zhang, A review of precious-metal-free bifunctional oxygen electrocatalyst: rational design and application in Zn–air batteries, *Adv. Funct. Mater.*, 2018, **28**, 1803329.

13 S.-K. Singh, K. Takeyasu and J. Nakamura, Active sites and mechanism of oxygen reduction reaction electrocatalysis on nitrogen-doped carbon materials, *Adv. Mater.*, 2019, **31**, 1804297.

14 G.-N. Li, J.-J. Zhang, W.-S. Li, K. Fan and C. J. Xu, 3D interconnected hierarchical porous N-doped carbon constructed by flake-like nanostructure with Fe/Fe_3C for efficient oxygen reduction reaction and supercapacitor, *Nanoscale*, 2018, **10**, 9252–9260.

15 J.-C. Li, P.-X. Hou, M. Cheng, C. Liu, H.-M. Cheng and M.-H. Shao, Carbon nanotube encapsulated in nitrogen and phosphorus co-doped carbon as a bifunctional electrocatalyst for oxygen reduction and evolution reaction, *Carbon*, 2018, **139**, 156–163.

16 Q.-Q. Zhang, Z.-Y. Duan, Y. Wang, L.-N. Li, B. Nan and J.-Q. Guan, Atomically dispersed iridium catalysts for multifunctional electrocatalysis, *J. Mater. Chem. A*, 2020, **8**, 19665–19673.

17 X. He, H. Sun, M. Zhu, M. Yaseen, D. Liao, X. Cui, H. Guan, Z. Tong and Z. Zhao, N-Doped porous graphitic carbon with multi-flaky shell hollow structure prepared using a green and 'useful' template of $CaCO_3$ for VOC fast adsorption and small peptide enrichment, *Chem. Commun.*, 2017, **53**, 3442–3445.

18 R. Thangavel, A. G. Kannan, R. Ponraj, V. Thangavel, D.-W. Kim and Y.-S. Lee, Nitrogen- and sulfur-enriched porous carbon from waste watermelon seeds for high-energy, high-temperature green ultracapacitors, *J. Mater. Chem. A*, 2018, **6**, 17751–17762.

19 L. Bai, Z.-Y. Duan, X.-D. Wen, R. Si, Q.-Q. Zhang and J.-Q. Guan, Highly dispersed Ruthenium-based multifunctional electrocatalyst, *ACS Catal.*, 2019, **9**, 9897–9904.

20 J. Shui, M. Wang, F. Du and L. Dai, N-doped carbon nanomaterials are durable catalysts for oxygen reduction reaction in acidic fuel cells, *Sci. Adv.*, 2015, **1**, e1400129–e1400135.

21 D. Guo, R. Shibuya, C. Akiba, S. Saji, T. Kondo and J. Nakamura, Active sites of nitrogen-doped carbon materials for oxygen reduction reaction clarified using model catalysts, *Science*, 2016, **351**, 361–365.

22 L. Zhang and Z. Xia, Mechanisms of oxygen reduction reaction on nitrogen-doped graphene for fuel cells, *J. Phys. Chem. C*, 2011, **115**, 11170–11176.

23 T. Wang, Z.-X. Chen, Y.-G. Chen, L.-J. Yang, X.-D. Yang, J.-Y. Ye, H.-P. Xia, Z.-Y. Zhou and S.-G. Sun, Identifying the active site of N-doped graphene for oxygen reduction by selective chemical modification, *ACS Energy Lett.*, 2018, **3**, 986–991.

24 C. M. Cordeiro and M. T. Hincke, Recent patents on eggshell: shell and membrane applications, *Recent Pat. Food, Nutr. Agric.*, 2011, **3**, 1–8.

25 C.-H. Hsu, Z.-B. Pan, C.-R. Chen, M.-X. Wei, C.-A. Chen, H.-P. Lin and C.-H. Hsu, Synthesis of multiporous carbons from water caltrop shell for high-performance supercapacitors, *ACS Omega*, 2020, **5**, 10626–10632.

26 M. Li and J. Xue, Integrated synthesis of nitrogen-doped mesoporous carbon from melamine resins with superior performance in supercapacitors, *J. Phys. Chem. C*, 2014, **118**, 2507–2517.

27 M. K. Rybarczyk, M. Lieder and M. Jablonska, N-doped mesoporous carbon nanosheets obtained by pyrolysis of a chitosan–melamine mixture for the oxygen reduction reaction in alkaline media, *RSC Adv.*, 2015, **5**, 44969–44977.

28 Z. Liu, Z. Du, H. Song, C. Wang, F. Subhan, W. Xing and Z. Yan, The fabrication of porous N-doped carbon from widely available urea formaldehyde resin for carbon dioxide adsorption, *J. Colloid Interface Sci.*, 2014, **416**, 124–132.

29 F. Marquez-Mntesino, N. Torres-Figueredo, A. Lemus-Santana and F. Trejo, Activated carbon by potassium carbonate activation from pine sawdust, *Chem. Eng. Technol.*, 2020, **43**, 1716–1725.

30 A. C. Lua and J. Guo, Activated carbon prepared from oil palm stone by one-step CO_2 activation for gaseous pollutant removal, *Carbon*, 2000, **38**, 1089–1097.

31 A. Aworn, P. Thiravetyan and W. Nakbanpote, Preparation of CO_2 activated carbon from corncob for monoethylene glycol adsorption, *Colloids Surf., A*, 2009, **333**, 19–25.

32 J. Cao, C. Zhu, Y. Aoki and H. Habazaki, Starch-derived hierarchical porous carbon with controlled porosity for high performance supercapacitors, *ACS Sustainable Chem. Eng.*, 2018, **6**, 7292–7303.

33 Z. Li, D. Li, Z. Liu, B. Li, C. Ge and Y. Fang, Mesoporous carbon microspheres with high capacitive performances for supercapacitors, *Electrochim. Acta*, 2015, **158**, 237–245.

34 G.-S. Li and Y.-G. Zhang, Highly selective two-electron oxygen reduction to generate hydrogen peroxide using graphite felt modified with N-doped graphene in an electro-Fenton system, *New J. Chem.*, 2019, **43**, 12657–12667.

35 T. Wang, Z.-X. Chen, Y.-G. Chen, L.-J. Yang, X.-D. Yang, J.-Y. Ye, H.-P. Xia, Z.-Y. Zhou and S.-G. Sun, Identifying the active site of N-doped graphene for oxygen reduction by selective chemical modification, *ACS Energy Lett.*, 2018, **3**, 986–991.

36 C. Tang, H.-F. Wang and Q. Zhang, Multiscale principles to boost reactivity in gas-involving energy electrocatalysis, *Acc. Chem. Res.*, 2018, **51**, 881–889.

37 Y.-C. Chen, T. Asset, R. Lee, K. Artyushkoya and P. Atanassov, Kinetic isotopic effect studied of iron–nitrogen–carbon electrocatalysts for oxygen reduction reaction, *J. Phys. Chem. C*, 2019, **123**, 11476–11483.

38 M. K. Ravikumar and A. K. Shukla, Effect of methanol crossover in a liquid-feed polymer-electrolyte direct methanol fuel cell, *J. Electrochem. Soc.*, 1996, **143**, 2601–2606.

39 N. Jung, Y.-H. Cho, M. Ahn, J. W. Lim, Y. S. Kang, D. Y. Chung, J. Kim, Y.-H. Cho and Y.-E. Sung, Methanol-tolerant cathode electrode structure composed of heterogeneous composites to overcome methanol crossover effects for direct methanol fuel cell, *Int. J. Hydrogen Energy*, 2011, **36**, 15731–15738.

40 X. Wang, Z. Li, Y. Qu, T. Yuan, W. Wang, Y. Wu and Y. Li, Review of metal catalysts for oxygen reduction reaction: From nanoscale engineering to atomic design, *Chem*, 2019, **5**, 1486–1511.

41 B. Lu, Z.-Y. Duan, X.-D. Wen, R. Si and J.-Q. Guan, Atomically dispersed manganese-based catalysts for efficient catalysis of oxygen reduction reaction, *Appl. Catal., B*, 2019, **257**, 117930.

42 F. Cheng and J. Chen, Metal–air batteries: from oxygen reduction electrochemistry to cathode catalysts, *Chem. Soc. Rev.*, 2012, **41**, 2172–2192.

43 Z. L. Wang, D. Xu, J. J. Xu and X. B. Zhang, Oxygen electrocatalysts in metal–air batteries: from aqueous to nonaqueous electrolytes, *Chem. Soc. Rev.*, 2014, **43**, 7746–7786.

44 Y. S. Liu, Q. Sun, W. Z. Li, K. R. Adair, J. Li and X. L. Sun, A comprehensive review on recent progress in aluminum-air batteries, *Green Energy Environ.*, 2017, **2**, 246–277.

45 R. Mori, Recent developments for aluminum–air batteries, *Electrochem. Energy Rev.*, 2020, **3**, 344–369.